Overturn study in the moon thermal evolution

In the context of Geophysics lectures supervised by T.Alboussière, C. Michaut, S.Labrosse

CONTENTS

INTRODUCTION

I. Moon Formation

This study focuses on the thermal overturn of the Moon's cumulate mantle at the beginning of the second cooling phase. The Moon formed approximately 4.5 billion years ago from a collision between two planetary bodies: the proto-Earth and Theia, a planetary body similar in size to Mars. The impact between the two bodies was violent enough that, once most of the ejected matter aggregated into a single body (the Moon), its mantle was completely melted, forming a Lunar Magma Ocean (LMO) extending from the core to the surface (see Figure 1.1).
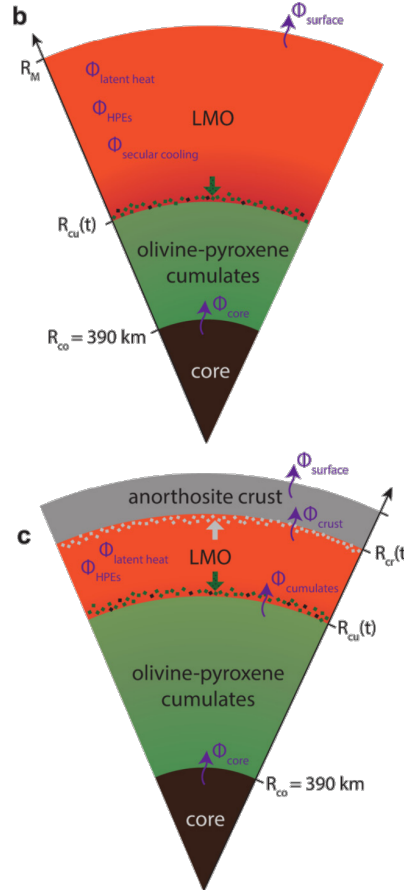

Figure 1.1 – Lunar mantel structure during the first radiative cooling phase (**a**) and the second diffusive cooling phase (**b**), from Colin and al. from [1]

II. Moon cooling

The cooling of the Moon occurred in two phases: a short one ($\approx$ 1000 years), driven by radiative processes, and a much longer one, driven by diffusive processes.

A. First Radiative step

During the first step, a deposit of olivine and pyroxene solidified at the interface between the LMO and the solid core. Once the LMO surface reached the eutectic temperature, an anorthosite crust formed, blocking radiative losses. The main cooling process then became diffusion, with a much longer timescale compared to radiative loss.

During the radiative cooling phase, a common hypothesis is to consider that the temperature of the LMO corresponds to the liquidus temperature from the binary phase diagram of olivine-pyroxene/anorthosite. The temperature of the LMO follows the cooling path of this diagram. The LMO temperature is, therefore, directly related to the fusion temperature of olivine through the following equation:

$$T_{\text{liq}} = T_{\text{ol}} - mC(t)$$

Where $C(t)$ is the mass fraction in anorthite component and T_{liq}, T_{ol} are, respectively, the temperature of the liquidus and the fusion temperature of olivine.

Considering the fact that anorthite is not present in the olivine-pyroxene cumulates, the conservation of anorthite in the LMO yields, for a given time t:

$$(R_M^3 - R_{co}^3)C_0 = (R_M^3 - R_{cu}^3)C(t)$$

Combining the two previous equations, we finally obtain the following liquidus temperature evolution. Ignoring diffusive processes due to the short timescale and considering this temperature constant in the first phase leads to an isentropic temperature profile (see Figure 1.2):

$$T_{Liq}(t) = T_{OL} - mC_0 \frac{Rm^3 - R_{co}^3}{R_m^3 - R_{cu}^3(t)}$$

$$(1.1)$$

B. Second diffusive step

Once the eutectic temperature is reached, the anorthosite crust begins to form, significantly reducing radiative heat dissipation. This marks the end of the first cooling step and the beginning of the second.

The isentropic temperature profile obtained in (1.1) leads to instabilities in the second phase, ultimately resulting in a thermal overturn in the cumulates. At the end of the first phase, there is an accumulation of cold matter at the top of the cumulates, while the cumulates near the core interface remain much hotter. The temperature difference is on the order of $500K$. Logically, the colder, denser cumulates will try to move beneath the hotter, lighter ones, leading to the overturn.
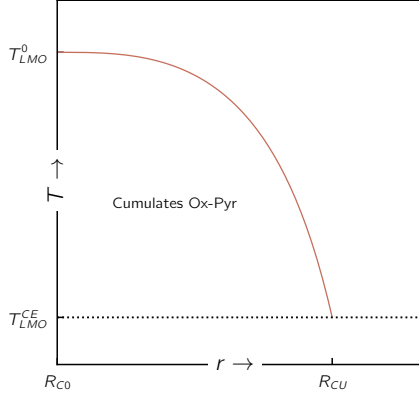
Andrea Combette | Louis Poitevin

Figure 1.2 – Isentropic temperatures profiles corresponding to 1.1 reached after the end of the first cooling stage, leading to overturn in the cumulates and increasing flux.

The dynamic in the solid cumulates at the beginning of the second phase can be described using the Boussinesq approximation in a slab geometry, where all the thermodynamic variables are considered constant except the temperature T, the pressure P and the density ρ multiplied by g.

$$\begin{cases} \vec{\nabla} \cdot \vec{u} = 0 \\ \rho_0 \frac{\partial \vec{u}}{\partial t} + \vec{u} \cdot \vec{\nabla} \vec{u} = \vec{\nabla} P + \eta \nabla^2 \vec{u} + \rho \vec{g} \\ \frac{\partial T}{\partial t} + \vec{u} \cdot \vec{\nabla} T = \kappa \nabla^2 T \\ \rho = \rho_0 (1 - \alpha(T - T_0)) \end{cases}$$

As a thermal conductivity driven Rayleigh-Bénard convection is expected, the rescaling is chosen with respect to the diffusive characteristic time d^2/κ, leading to the following rescaling :

$$\hat{x}, \hat{y} = \frac{x}{d}, \frac{y}{d}, \quad \hat{z} = \frac{z}{d} + \frac{1}{2}, \quad \hat{\theta} = \frac{\theta}{\Delta T},$$

$$\hat{t} = \frac{t\kappa}{d^2}, \quad \hat{p} = \frac{pd^2}{\kappa\eta}$$

with d the height of the cumulates layer (e.g. $R_{cu} - R_{co}$), ΔT the temperature difference between the LMO/cumulates interface and the core/cumulates interface, κ the thermal diffusivity of the cumulates and η its viscosity. When we considered the density and the heat capacity equal in the crust, in the LMO and in the cumulates. We can show that

$$\kappa_{cu} = \frac{k_{cu}}{\rho c_p} = 1.2e^{-6} m^2 s^{-1}$$

To get the correct dimensionnalized value we will use the following parameters values :

d	κ	ΔT
$1e^6$ m	$1.2e^{-6} m^2 s^{-1}$	550 K

Table 1.1 – Cumulates width, heat diffusivity and characteristic temperatures difference, from [1]

This rescaling results in the following dimensionless formulation of equations.

$$\begin{cases} \vec{\nabla} \cdot \vec{u} = 0 \\ \frac{1}{Pr} \frac{Du}{Dt} = -\vec{\nabla} p + \nabla^2 \vec{u} + Ra\theta \vec{e}_z = 0 \\ \frac{D\theta}{Dt} = \nabla^2 \theta \end{cases}$$

$$(1.2)$$

With $Ra = \frac{\rho_0 g \alpha \Delta T d^3}{\kappa\eta}$ and $Pr = \frac{\eta}{\kappa\rho_0}$. The cumulates being a solid phase, the Prandlt number can be considered infinite, simplifying again the system, leading to the final formulation of our problem :

$$\begin{cases} \vec{\nabla} \cdot \vec{u} = 0 \\ 0 = -\vec{\nabla} p + \nabla^2 \vec{u} + Ra\theta \vec{e}_z \\ \frac{D\theta}{Dt} = \nabla^2 \theta \end{cases}$$

$$(1.3)$$

Regarding boundary conditions, we will consider free-slip contact between the cumulate layer and its boundaries (the LMO and the core) with impermeability. For this study we will neglect the thermal flux from the core and we will consider the temperature of the LMO boundary constant ;

$$\begin{cases} \vec{u} \cdot \vec{e}_z = 0 \text{ on } z = 0, 1 \\ \frac{\partial \theta}{\partial z} = 0 \text{ on } z = 0 \\ \tau^x = 0 \text{ on } z = 0, 1 \\ \theta = 0 \text{ on } z = 1 \end{cases}$$

The goal of this project is to study the evolution of the cumulate layer at the beginning of the second stage of the Moon's cooling, focusing on the effects of temperature profiles and the range of Rayleigh numbers Ra.

III. Numerical Implementation

For the numerical implementation, we utilized the Dedalus [2] toolbox. A Fourier and Chebyshev spectral method was applied to solve the convection-diffusion equations. The Fourier decomposition was applied to the x-axis, characterized by periodic boundary conditions on a regularly spaced grid of 256 points:

$$x_j = j\frac{L}{N}$$

For the z-direction, we employed the Chebyshev spectral method to satisfy the

Dirichlet boundary conditions applied to the temperature. This was achieved using the Chebyshev-Gauss-Lobatto collocation points to avoid the so-called Runge's phenomenon:

$$z_j = \cos\left(j\frac{2\pi}{N}\right)$$

For time integration, we used a second-order Runge-Kutta scheme with adaptive time-stepping applied every 10 iterations.

Another important point to note is the introduction of instability to provoke the overturn. This was achieved using simple Gaussian noise damped at the walls. The noise could significantly influence the modal response of the system and the characteristic lengths, which we will analyze further.

IV. Objectives

Due to the spherical coordinates, the initial temperature profile scales as $\propto \frac{1}{r^3}$. To study this within a slab Cartesian system, we approximated the profile with a piece wise linear model. This approach highlights the importance of the depth of the linear part in determining the dynamics of the system.

Additionally, in [1], the overturn is assumed to follow the relationship:

$$\Phi_{OV} \sim e^{-\frac{t}{\tau_{OV}}}$$

We aim to evaluate this hypothesis and examine the influence of the Rayleigh number on the system's dynamics within a Moon-compatible range ($Ra \approx 10^5 \sim 10^6$).

DEPTH STUDY

I. Control parameters : e and Ra

The Rayleigh-Bénard instability is usually studied under conditions of a linear temperature gradient between the "hot" and "cold" sides of the observed volume. However, the temperature profile at the beginning of the second phase in the cumulate varies as $\propto 1/r^3$. Therefore, using a linear temperature profile is not well-suited in this case.

To study the effect of the "shape" of the initial temperature profile, we used a piece wise function defined in Equation 2.1. The main goal of this study is to understand the effect of the depth, e, which represents the depth of the instability-contributing layer, and to determine if the linear gradient approximation yields results that are sensibly close to those of a more realistic model. The choice of this piece wise model was motivated by its flexibility to define a "curvature" approximating the $1/r^3$ profile while

Andrea Combette | Louis Poitevin

easily controlling the energy associated with any depth e.

$$T(z, e) = \begin{cases} \frac{L_z - z}{e(2-e)} & z > L_z - e \\ \frac{L_z}{2L_z - e} & z < L_z - e \end{cases}$$

$$(2.1)$$

To allow for a correct comparison between the results, the profiles were tuned to all have the same initial internal energy. This was achieved by controlling the core temperature with the following relation:

$$T(0, e) = \frac{L_z}{2L_z - e}$$

$$(2.2)$$

Ten profiles were used, ranging from a shallow depth ($e = 0.1L_z$) to a linear profile. The shapes of the initial thermal profiles are displayed in Figure 2.1
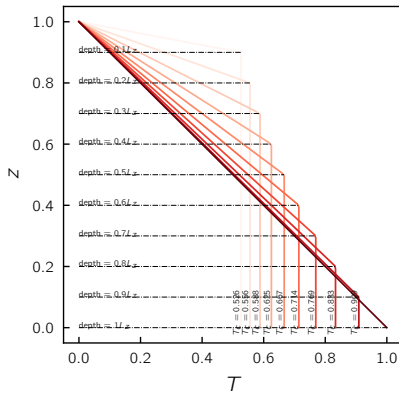

Figure 2.1 – Initial thermal profiles used in the simulations with the associated core temperature ensuring constant initial energy.

A second control parameter was used in the simulation: the Rayleigh number (Ra). Two different values were used to simulate two sets of e-dependent data: $Ra = 7.10^4$ and $Ra = 7.10^5$. Several arguments motivated the choice of two distinct values for the study of the influence of e. First, the Moon-compatible range includes fairly high Ra values, which significantly increase computation time. Additionally, it was interesting to study a case at lower Ra, as the dynamics of the overturn should be comparable to those at higher Ra values. Furthermore, we found that two different regimes of instability arise for the two chosen values. Below a specific threshold of Ra, the instability remains in a decaying-steady-state (DSS) with an almost constant wavelength.
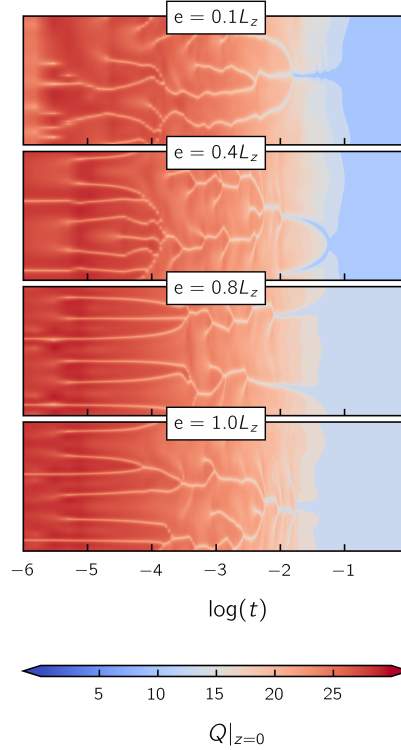

Figure 2.2 – Surface heat flux as a function of time. Top: $Ra = 7.10^4$, Bottom = $Ra = 7.10^5$
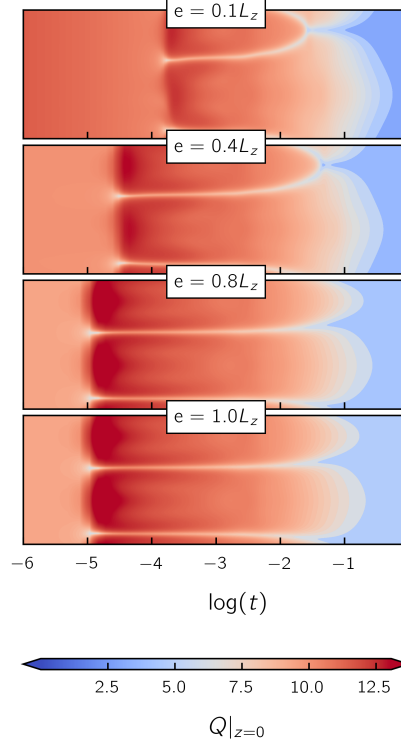

Figure 2.3 – Surface heat flux as a function of time. Top: $Ra = 7.10^4$, Bottom = $Ra = 7.10^5$

If Ra exceeds this threshold, which determines the boundary between the two unstable regimes, the convection forces a constant modification of the wavelength through the fusion and division of the convective rolls. The choice of the two exact Ra values used in the simulation was made arbitrarily with respect to the two regimes, as only the difference between the regimes is significant here and not the exact Ra values. As shown in Figures 2.3 and 2.2, the choice of the two Ra values is appropriate, as the two regimes are clearly exhibited: 2.3-top: DSS; 2.2-bottom: competition between multiple overturns and instability decay.

II. Influence of e on the overturn

Due to the specific arrangement of the cumulates at the end of the first stage (cold on top and hot below), a thermal overturn is inevitable (see Figure 2.4). After a given amount of time, allowing the system to reach the required conditions to effectively start convection, the hot matter abruptly rises while the cold matter sinks, resulting in a thermal overturn: an inversion of the cold and hot regions within the cumulates. Once the instability starts, it does not stop until the effective Ra number falls below the critical stability value due to the cooling of the system.

The thermal overturn is, of course, clearly visible on a thermal map, as displayed in Figure 2.4. However, it is also significant to examine the local heat flux map (see Figure 2.5). The overturn appears as a cell of very high heat flux, a characteristic that will be studied later on.

The influence of the control parameter e is straightforward: the larger the instability-contributing region is, the sooner the overturn takes place, the quicker it is, and the more powerful the heat flux cell becomes.

A. overturn dynamics

The temperature and internal heat flux maps are effective for understanding the temporality of the phenomenon, but they are not very practical for measuring quantitative times to characterize the effect of e on the overturn dynamics. We chose to use two dimensionless numbers for this purpose: the Reynolds number (Re) and the Nusselt number (Nu). The Reynolds number compares viscous forces to inertial forces. It can also be interpreted as the ratio between the characteristic times of diffusive momentum transport and convective momentum transport. In essence, it provides

Andrea Combette | Louis Poitevin

information on the dynamics of the system. The Nusselt number, on the other hand, compares thermal diffusion time to thermal convection time and therefore informs on the thermal behavior of the system.

The first result extracted from the simulation is that the choice of the shape of the initial temperature profile—hence the choice of depth—does not significantly affect the amount of energy lost by the system over the entire duration of the simulation. The average temperature profiles are similar enough to neglect the impact of e on the global cooling of the system (see Figure 2.6, top). However, it directly and significantly affects the timing, duration, and intensity of the overturn. This is a significant result as the overturn is very localized in time. Moreover, the energy it transports is tremendous. Depending on the dynamics of the overturn, it can delay solidification or even re-melt the crust and mantle.

The two numbers, Re and Nu, provide insights into the kinematics of the phenomenon. As Nu represents a ratio of thermal diffusion to convection, the sharp increase visible in Figure 2.6-bottom indicates the overturn event. The latter part of the peak is dominated by an increase in conduction and a reduction in convection due to the cooling of the system, which slows down the instability. While Nu primarily informs on the thermal aspects of the phenomenon, Re provides insights into the transport of momentum within the cumulates. Several peaks are visible in Figure 2.6-middle. Each peak is correlated with the separation or fusion of convective rolls. The separation is caused by a secondary overturn, as will be explained in the modal analysis (see Section II), while the fusion occurs due to the system's inability to maintain the rolls as it cools. To quantify any peaks, we used three characteristic times: the left and right half-height times and the peak time. The depth e controls the Nu and Re times almost identically (see Figure 2.7), with differences being mostly noticeable for small e. Although no model has been established to determine the exact relationship between these times and e, two behaviors arise from this result: the deeper e is, the sooner the overturn takes place and the shorter it lasts. However, a "saturation" effect also appears. For deep profiles ($e \geq 0.7$), all three times converge toward the limit of the purely linear thermal profile. Figure 2.7 also confirms what can be observed in Figure 2.6: the Nu peak always occurs later than the Re peak, although a synchronization is evident—the maximum of Re coincides with the Nu left
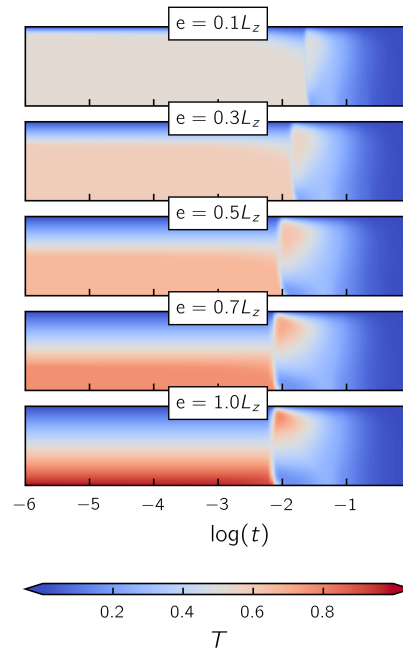
time.

Figure 2.4 – Evolution of the thermal profile with time in function of e for $Ra = 7.10^4$. The overturn is clearly visible for all e at $t \approx 10^{-2}$
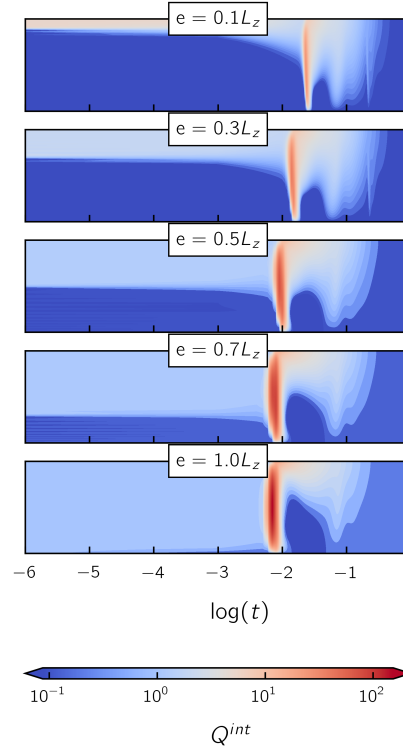

Figure 2.5 – Evolution of the local heat flux with time in function of e for $Ra = 7.10^4$. The overturn, characterized by a heat cell, is clearly visible for all e at $t \approx 10^{-2}$

This can be understood as follows: to achieve an increase in heat flux (Nu), matter must first be transported, with convection being the preferred heat transport mechanism during the overturn.

The other main effect of e on the overturn dynamics is on the energy transported during the event. Three measures are relevant here: the local heat flux (Q_{max}^{int}) generated by the overturn, the overall energy dissipated within the cumulates (E_{ov}^{cu}), and the energy lost in the LMO (E_{ov}^{lib})
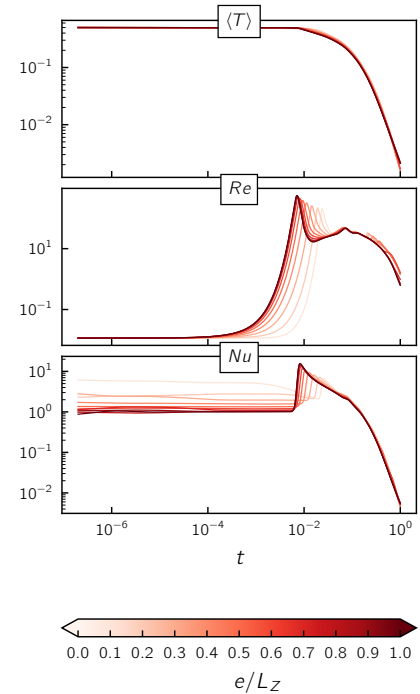

Figure 2.6 – Top : average temperature - Middle : Reynolds number - Bottom : Nusselt number. Quantities measured for all e at $Ra = 7.10^4$
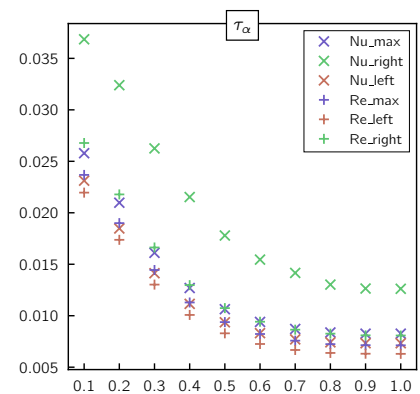

Figure 2.7 – Characteristic times of the main peak (overturn peak) for both Nu and Re

Andrea Combette | Louis Poitevin

Figure 2.8 displays the maximum local heat flux recorded during the simulation as a function of depth e. While the exact mathematical relationship remains unclear, it is interesting to note that this quantity scales perfectly linearly with e. This linear dependency is observed again when integrating the local heat flux with respect to the width of the Re peak, which approximately corresponds to the energy dissipated by the overturn within the cumulates. The choice of this integration window is explained by the dynamics of the overturn: heat transport begins at the bottom of the Re peak, and convection remains predominant until the peak of the Nu curve, which coincides with the right half-time of the Re peak. Thus, the width of the Re peak can be considered a suitable integration window for the overturn. Figure 2.9 confirms this linear relationship, with slight non-linearity at shallow and deep values of e. The significant deviation at low e can be explained by the complex shape of the overturn peak for "high" Ra values, as displayed in Figure 2.10. Nonetheless, the deeper e is, the more energy is transported by the overturn within the cumulates.
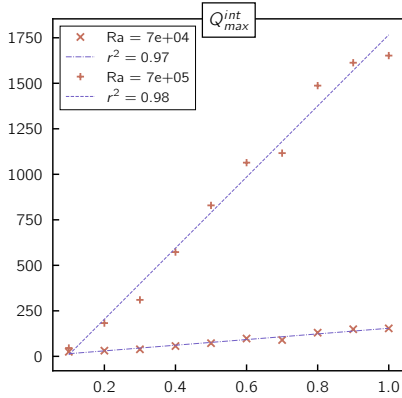

Figure 2.8 – Maximum local heat flux as a function of e. The dashed lines are linear fit. For $Ra = 7.10^4$, we found : $Q_{max}^{int}(e) = -0.9738 + 155.29e$ and for $Ra = 7.10^5$; $Q_{max}^{int}(e) = -186.6 + 1952.7e$

On the other hand, Figure 2.11 shows that e has no significant effect on the energy released in the LMO. This indicates a decoupling of the two phenomena, which aligns with the behavior of the average temperature in Figure 2.6: the amount of energy lost is independent of e.
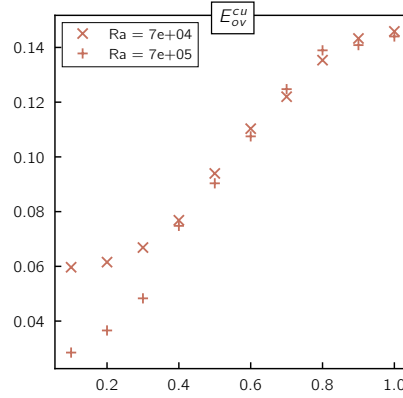

Figure 2.9 – Energy dissipated in the cumulates during the overturn.

III. Influence of Ra

We showed that the shape of the initial thermal profile controls the dynamics of the overturn but has no effect on the warming of the LMO. In this section, we will demonstrate that the choice of Ra has a significant impact on the dynamics of the overturn.
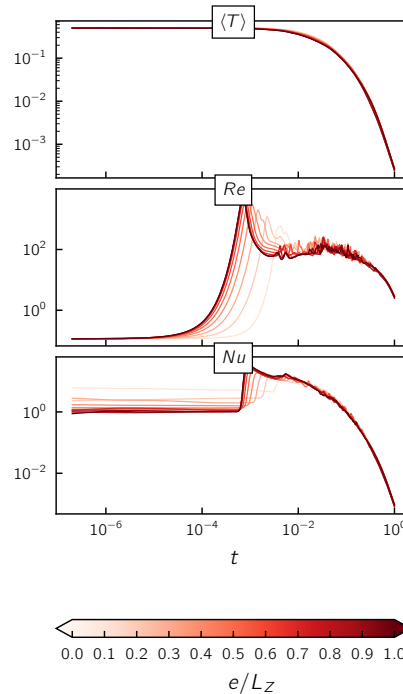

Figure 2.10 – Top : average temperature - Middle : Reynolds number - Bottom = Nusselt number. Quantities measured for all e at $Ra = 7.10^5$

The Rayleigh-Bénard instability, as presented in this work, exhibits two regimes once started: a decaying-steady-state (DSS) and a non-stationary

one. The non-stationary case is represented in Figure 2.2. In this regime, cells are unstable and undergo a second overturn, dividing the wavelength by three (more explanation on this behavior is provided in Section II). Due to cooling, cells also tend to widen and merge with their smaller neighbors until no cells remain. These are competing mechanisms. These events can be observed in Figure 2.10, and traces can also be seen in the heat flux map (Figure 2.12), though none appear in the temperature map. While the order of magnitude of the different scalar quantities extracted from the simulation differs, the global behavior of the overturn and cooling is not affected by this choice of a higher Ra. The results presented above still hold.
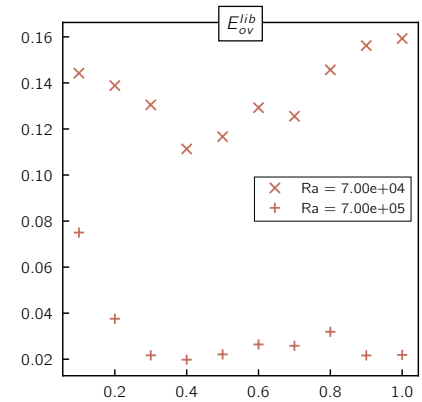

Figure 2.11 – Energy dissipated in the LMO by the overturn

The data presented in Figures 2.8, 2.9, and 2.11 show a deviation in behavior compared to the data obtained from the lower Ra simulation. However, these deviations are not completely reliable as a higher numerical error was observed in this data, especially at low e.

Regarding the effects of Ra on the dynamics of the overturn, they can be summarized in three points: The higher Ra is, the faster the overturn occurs and the shorter it lasts. Ra has no effect on the amount of energy dissipated within the cumulates. The instantaneous power density increases with Ra but is compensated by the shorter duration of the event, preventing an excessive release of energy in the LMO. The amount of energy released in the LMO is inversely proportional to Ra.

IV. Reel time re-scaling

This study was conducted using dimensionless quantities, but the goal was to compare the effects of the shape of

Andrea Combette | Louis Poitevin

the initial thermal profile on the entire dynamics of lunar cooling with existing literature. The study at low Ra was relevant for understanding the mechanisms at play; however, this low Ra is far from the Moon-compatible range. This statement also motivated the choice of a second Ra, with a compatible value of 7.10^5. Our main results are presented in Tables 2.1 and 2.2. The re-scaling of the energy was carried out as presented in Equation 2.3.

$$E = \int\int \langle\Phi\rangle dzdt$$
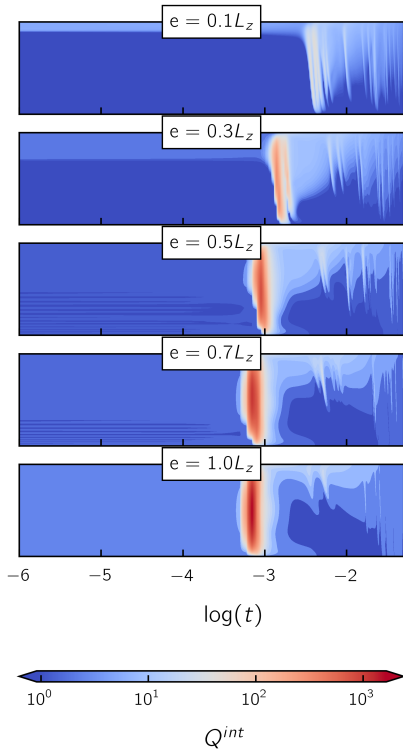$$= \frac{d^2\Delta T}{\kappa}\int\int \langle\hat{\Phi}\rangle d\hat{z}d\hat{t}$$

(2.3)

Figure 2.12 – Evolution of the local heat flux with time in function of e for $Ra = 7.10^5$

	e	time (Myr)
τ_{ov}	0.1	23
τ_{ov}	1	115
$\Delta\tau_{ov}$	0.1	4,5
$\Delta\tau_{ov}$	1	35

Table 2.1 – Overturn date (τ_{ov}) and duration ($\Delta\tau_{ov}$). The overturn date is defined as the time of the Nu peak. The duration is defined as the width of the Re peak.

	Energy ($10^{19}J$)
E_{ov}^{lib}	6,72
E_{ov}^{cu}	6,3

Table 2.2 – Energy liberated into the LMO (E_{ov}^{lib}) and dissipated into the cumulates during the overturn (E_{ov}^{cu})

RAYLEIGH STUDY

In this section, we will emphasize the importance of the Rayleigh number regarding the cooling dynamics of the Moon through scaling laws and modal analysis.

I. Convective Behavior

When we consider the super-isentropic temperature profile, the overturn dynamics should initially be dominated by convective processes due to the dominant buoyancy force in the presence of the random noise we introduced. Hence, the overturn time and characteristics should depend on the Rayleigh number on short time scales.
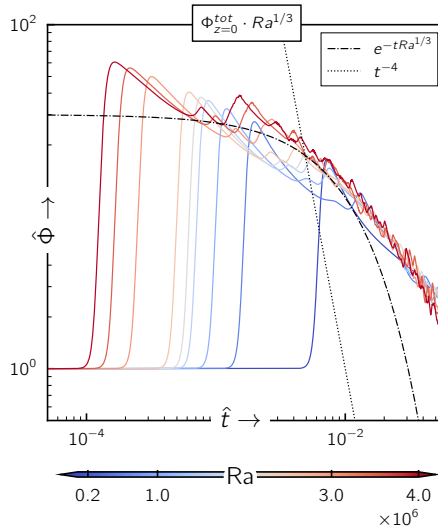
Figure 3.1 – Adimensionnalized Total flux time evolution for multiple Rayleighs values. The rescaled time from 1.1 yield an overturn time of the order of 1 or 100-Myr. The plain black and dotted line are characteristic decaying scaling we will unearth firther.

A. Time Rescaling

More precisely, we expect the overturn time τ_{OV} to be inversely proportional to Ra. Indeed, we should have:

$$\tau_{OV} \sim \tau_{conv} = Ra^{-1}\tau_{diffusion}$$

(3.1)

To uncover this scaling, we will study the total flux at the top boundary of the system:

$$\Phi_{tot}(z=0) = V\theta - \partial_z\theta$$

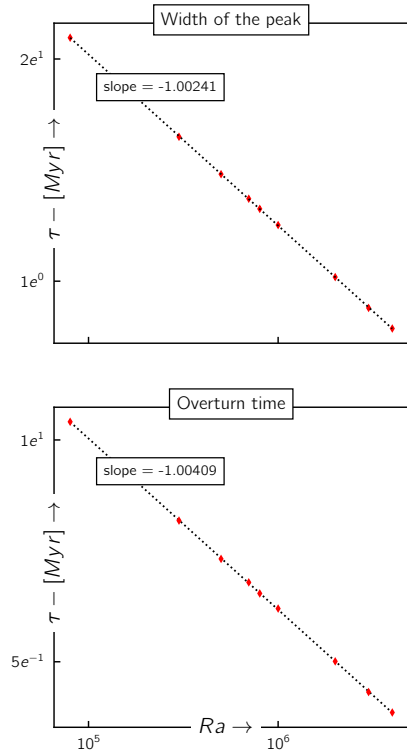This flux includes both the advective and diffusive contributions.

Figure 3.2 – The top loglog plot stands for Rayleighs evolution of the overturn peak width and th bottom plot fot the time of the overturn dependency over the Rayleigh. Both exhibit a perfect inversely proportional dependency over the Raleigh

This overturn time is significantly larger than the one expected in previous studies [1]. Indeed, it is traditionally accepted that the overturn time should be on the order of several thousand years, which allowed neglecting the diffusive behavior in the cumulates during the first cooling stage. However, this result is strongly dependent on the noise level in the temperature profile. In our study, we considered a noise level of the order of $1e^{-3}T(z)$, which might be much more significant in the original cumulates.

Furthermore, the noise distribution is assumed to be normal, which could lead to slower responses for the natural modes of the system. These effects will be addressed further. We can already see that the exponential decay expected after the overturn is not evident and seems to be disrupted by a convection cascade that could accelerate the decay.

Andrea Combette | Louis Poitevin

The natural convective time scaling of the system is clearly illustrated in the following figure, where we studied the width and the time of the overturn phenomena.

We recover the expected dependency (3.1) for the overturn time. One interesting observation is the width dependency of the peaks. Indeed, it is also inversely proportional to Ra, meaning that for a non-negligible time after the overturn, the system is still dominated by convective behavior; otherwise, it would have been proportional to Ra.

Hence, since the convective behavior remains dominant after the overturn, there is no reason to expect an exponential decay characteristic of a diffusive process.
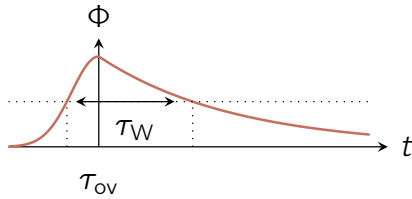

Figure 3.3 – A quasi-Gaussian peak with an exponential tail. The dashed line marks the peak time τ_{ov} The dotted horizontal line is at half maximum, illustrating how the width of the peak is measured.

B. Nusselt scaling

The total flux Φ_{tot} we studied earlier is equivalent in our study to the Nusselt number Nu at the top boundary. Indeed, Nu is classically defined as follows:

$$\text{Nu} = \frac{\Phi_{tot}}{\Phi_{cond}} = \frac{V\theta - \partial_z \Theta}{\partial_z \Theta}$$

However, in our study, we have impermeability at the boundary, which implies that the heat flux can only be diffusive, resulting in a constant Nu. In classical Rayleigh-Bénard steady convection (which is not the case here) at high Rayleigh numbers, we have the classical result Nu $\propto$ Ra$^{1/3}$, resulting from the equilibrium between diffusion in the boundary layer and heat transport by convection in the main flow. We can wonder if this result is still valid in our case for relatively short times, assuming that the temperature profiles will not be affected by diffusion.

Just after the overturn, a diffusive boundary layer will be maintained due to impermeability. In this diffusive boundary layer, we can assume that the temperature profile is linear (see fig.3.6). This gives:

$$\Phi_{z=0}^{tot} = \partial_z \theta = \frac{\Delta\theta}{\delta_T}$$

where δ_T is the size of the diffusive boundary layer. Assuming that the temperature difference does not depend on the Rayleigh number just after the overturn, we can deduce:

$$\Phi_{z=0}^{tot} \propto \frac{1}{\delta_T}$$

(3.2)

The hypothesis we made seems to be verified in fig.3.6, and it is perfectly reasonable since convective processes only advect heat. The size of the boundary layer is also an interesting subject and should scale like Ra$^{-1/3}$.

Indeed, if we equate the momentum diffusion and the temperature diffusion timescales in the boundary layer, we get for the momentum diffusion:

$$\tau_p = \eta/\Delta\rho\delta_T g$$

This is done by equating the buoyancy force with a typical Stokes friction. On the other hand, we get for the temperature diffusion:

$$\tau_T = \delta_T^2/\kappa$$

Equating both timescales, we easily get:

$$\delta_T \propto \text{Ra}^{-1/3}$$

(3.3)

This concludes our attempt to recover the desired scaling laws for the total flux (3.2), which matches the traditional Nusselt scaling. In fact, the adimensionalization we propose, combined with the same hypotheses we made, leads to:

$$\hat{\Phi} = \Phi\frac{d}{\Delta T} = \text{Nu}$$

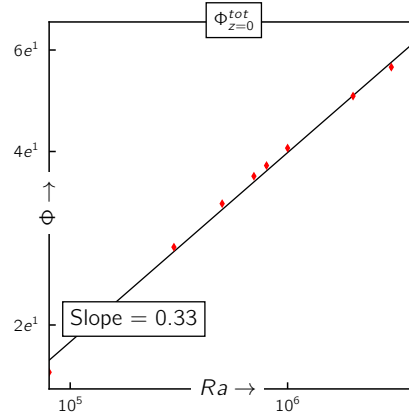Hence, it is quite reassuring to recover the same scaling.

Figure 3.4 – loglog plot of the Nusselt evolution over Ra at $t = \tau_{OV}$ the overturn time. We recover the 1/3 power scaling predicted by the previous approach

This scaling analysis of the convective overturn behavior allows us to propose the following natural rescaling for next studies :

$$\hat{t} = \text{Ra} \cdot t$$
$$\hat{\Phi} = \Phi \cdot \text{Ra}^{-1/3}$$

When convective processes are dominant this rescaling should unearth the same solution to (1.3) independently of the Rayleigh number. This can be verified on the next figure :
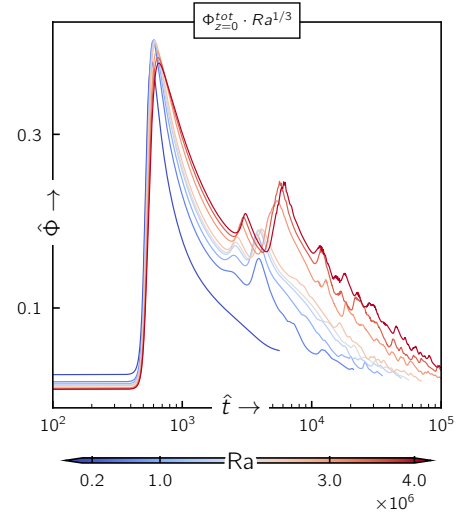

Figure 3.5 – Semilogy Rescaled total flux from different Rayleighs numbers. Clearly showing the dominant convective process at short time scale

We may wonder why the convective rescaling we used no longer works after the overturn. This is probably due to the dissipation, which becomes more significant for lower Ra in the boundary layer. Hence, we will no longer have $\Delta\theta$ independent of the Rayleigh number, which will break our previous scaling. Furthermore, the cascade of overturns we began to highlight previously I acts on decreasing scales with time, so it is not clear if the Rayleigh number we used to characterize the flow is still relevant.

C. Boundary Layer

We previously showed that during the overturn at time $t = \tau_{OV}$, we should have a boundary layer of size $\delta_T \propto \text{Ra}^{-1/3}$. This boundary layer results from an equilibrium between all the diffusive timescales and leads to another isentropic temperature profile. Hence, another overturn is expected to re-equilibrate the temperature profile. We can then easily understand that this

Andrea Combette | Louis Poitevin

will lead to an infinite cycle of overturn-diffusion-overturn processes, characterizing the overturn cascade we cited earlier.
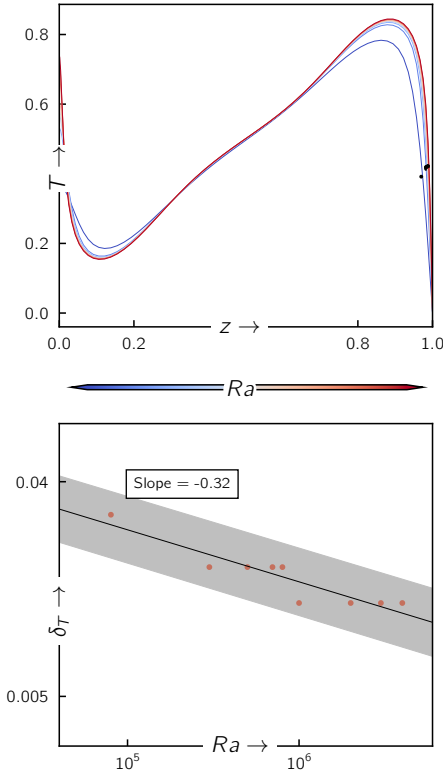

Figure 3.6 – On the top : Mean temperature profiles during the overturn ($\hat{t} = 600$) for several Rayleigh number with the boundary layer position indicated by black dots. *On the bottom* : Boundary layer width dependency over the Rayleigh number. The uncertainty raised by the discretization is represented by the grey field

We may wonder how this cascade will affect the Moon's cooling. Indeed, in a coarse approximation, we can assume that these successive overturns will lead to a well-mixed interior, thermally equilibrated over time. This assumption is verified in our simulations after the second overturn, as shown in fig.3.8. This thermalized assumption in the bulk allows us to neglect diffusive flux in the bulk and only consider the boundary layer flux. This leads to the following:

$$\Phi_{d-\delta}(t) \approx \Phi_{z=0}^{\text{tot}} = -k_{\text{cu}}\partial_z\theta \approx k_{\text{cu}}\frac{\theta(t)}{\delta_T(t)}$$

$$(3.4)$$

where k_{cu} is the heat conduction constant in the cumulates, and $T(t)$ is the temperature of the bulk. We will assume in the following that $\delta_T \ll d$, where d is the depth of the slab we studied.
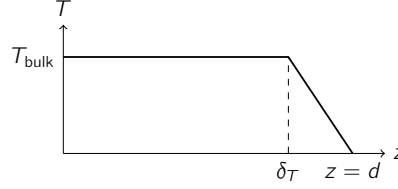

Figure 3.7 – Sketch of the temperature profile in a well-mixed situation

Now, if we consider the energy balance for the well-mixed interior, we can write, neglecting the advection (if we account for it, we can show that it has the same dependence in θ as the diffusive term since it is the boundary layer):

$$\frac{D\left(\rho C_p\langle\theta(t)\rangle H^2(d - \delta_T)\right)}{Dt} = -\Phi_z(t)H^2$$

$$\partial_t\left(\rho C_p\langle\theta(t)\rangle V\right) = -k\frac{\langle\theta(t)\rangle}{\delta_T}$$

The second step involves neglecting the boundary layer width while considering the bulk volume. This will finally lead to dropping the angles:

$$\partial_t\theta = -B\frac{\theta(t)}{\delta_t}$$

$$(3.5)$$

with $B = \frac{\kappa}{d}$. From now on, we will only focus on scalings; every constant will therefore be undefined. Now, considering that $\delta_T \propto \theta^{-1/3}$, which is a direct consequence of the study we did previously (3.2), we get:

$$\partial_t\theta = -A\theta^{4/3}$$

$$(3.6)$$

If we separate the variables, we easily obtain the following scaling for the temperature over time: $\theta(t) \sim t^{-3}$. This scaling will finally lead to the following expression for the total flux:

$$\phi_{z=0}^{\text{tot}} \sim t^{-4}$$

This power scaling is quite important and would result in a fast equilibration of the system. However, our simulations lead to a much slower cooling after the profile thermalization.

We previously state that the thermal boundary layer was temperature dependant, this power dependency was trying to include the effect of the convective behavior. However, if we consider the boundary layer independent of the bulk temperature (3.5) would results in the following scaling of the temperatures :

$$\theta(t) \sim \Phi_{z=0}^{\text{tot}} \sim e^{-\frac{\kappa t}{d\delta_T}}$$

$$(3.7)$$

We recover the characteristic diffusive slow decay was the one assumed in previous study [1]. This seems to match quite well the observed decay in our simulations with a characteristic time of decaying :

$$\tau_{\text{OV}} = \frac{d\delta_T}{\kappa}$$

This approximate decay is of the order of $1 - 10$ Myr matching the value taken by Collin [1] . However one can see that despite this scaling is quite interesting at long time it fails to describe the faster decaying of the Nusselt at short time, when the temperature profile is not thermalized in the bulk. In our adimensionalization with have :

$$\tau_{\text{OV}} = \frac{\kappa}{d^2}\frac{d\delta_T}{\kappa} = \text{Ra}^{-1/3}$$

$$(3.8)$$

The results have been plotted on fig.3.2, and one can see that the exponential decay is better than the power law, however it has the tendency to linearize at high time (typical from a power law). Hence, successive overturns seems to have a non negligible impact at large time on the cooling dynamics. To better understand this overturn cascade we should study the modes that are at stake in our study and their typical growing time.

II. Modal analysis

A. Linear perturbation theory

The observation we made in fig.3.8 is derived from the classic Rayleigh-Bénard linear perturbation analysis. We are interested here in the fastest growing mode of our study. In the literature, the most common use case of linear perturbation analysis applied to Rayleigh-Bénard convection is in the context of finding the "first" unstable mode at the onset of the instability ($\text{Ra} \gg \text{Ra}_c$).

This study generally depends on the boundary conditions we choose. Indeed, these will influence the sets of eigenfunctions describing our vertical dependencies. In our case, we have specific thermal boundary conditions that are not typical in the literature, with a perfectly insulating boundary layer at the bottom and a fixed temperature at the top. For the free-slip boundary, this is the general case that Rayleigh first used to propose his "normal mode."
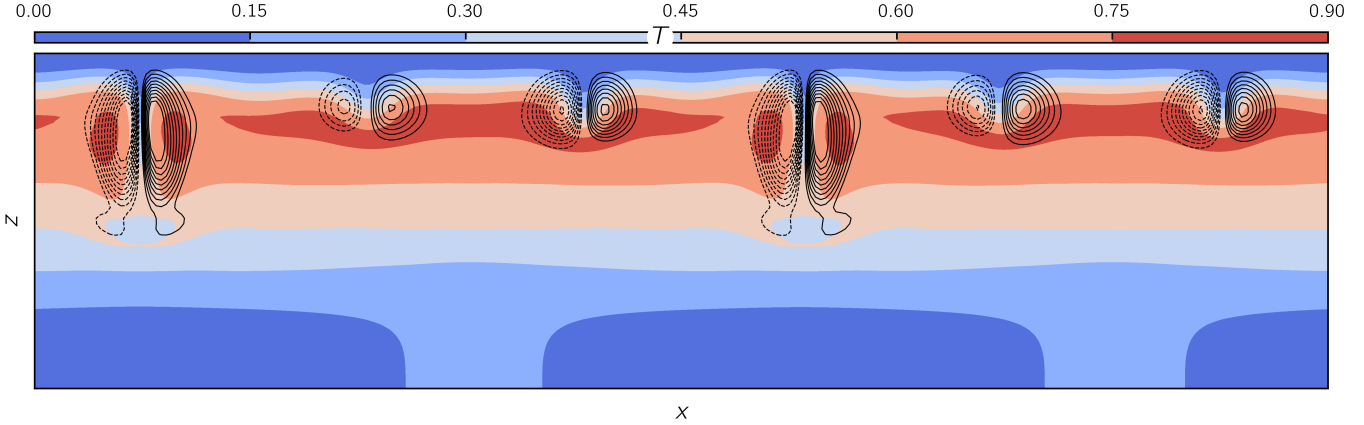
Andrea Combette | Louis Poitevin

Figure 3.8 – Contour plot of the Temperature field during the second overturn. The vorticty contour plots is superposed in blacked line to see the second instability rising at the top of the first overturn resulting structures. The wavelength of this structure seems to be exactly the double of the first overturn instability wavelength

Here, our problem is at the beginning of our study at a fixed Rayleigh number, beyond the critical Rayleigh number $R_c \approx 1700$. Hence, the question is: what is the preferred mode that has the fastest growth at our specific Rayleigh number? This is slightly different and will lead to different results than the "first" unstable mode study.

Indeed, if we consider the same adimensionalization as before with perturbed fields $(\theta^*, p^*, u_x^*, u_z^*)$ verifying:

$$\begin{cases} \theta(x,y,z,t) = \theta_s(z) + \theta^*(x,y,z,t), \\ p(x,y,z,t) = p_s(z) + p^*(x,y,z,t) \\ u_x(x,y,z,t) = u_x^*(x,y,z,t) \\ u_z(x,y,z,t) = u_z^*(x,y,z,t) \end{cases}$$

Taking the perturbed variables sufficiently small, this will lead to the following set of equation for infinite Prandtl :

$$\begin{cases} \vec{\nabla} \cdot \vec{u^*} = 0 \\ 0 = -\vec{\nabla} p^* + \vec{\nabla}^2 \vec{u^*} + \mathrm{Ra}\theta^* \vec{e}_z = 0 \\ \partial_t \theta^* = \vec{\nabla}^2 \theta^* + u_z^* \end{cases}$$

$$(3.9)$$

These equations are linear and symmetric in x and y, allowing us to use time dependant Fourier modes (a clean demonstration on how the leads to sinusoidal component of x,y is presented by [3]). Dropping the * and casting x,y as x, we get

$$(\theta, p, u_x, u_z) = (\Theta(z), P(z),$$
$$U(z), W(z)) e^{st} e^{iax}$$

$$(3.10)$$

Traditionally, we denote the remaining non-trivial derivative $\frac{d\cdot}{dz} \equiv D$. Furthermore, using (3.9) and taking two time

derivatives of the curl of the momentum equations [Pellew and Southwell], and using the conduction equation, we derived a single stability equation describing the flow:

$$-\Delta^2(\partial_t - \Delta)u_z = \mathrm{Ra}\Delta_1 u_z$$

$$(3.11)$$

with Δ_1 being the horizontal Laplacian (on x,y). Inserting the previous mode into (3.11) gives the following characteristic equation:

$$(D^2 - a^2)^2(D^2 - a^2 - s)W = -a^2 W \mathrm{Ra}$$

$$(3.12)$$

Now that we have described the flow, we need to see the impact of the boundary layer on the available sets of eigenfunctions W. Indeed, this part is rather tedious and requires a very careful study of the order of magnitude at stake. If the reader wants a detailed description of the manipulations involved, they should refer to (Drazin, Reid).

B. Boundary Conditions Characteristics

Regarding the impermeable free-slip boundary, this will lead to the following constraints:

$$W = D^2 W = 0 \,|\, z = -\frac{1}{2}, \frac{1}{2}$$

$$(3.13)$$

The first equality is evident, but it is not the case for the second. For the thermal boundary conditions, this is where our case is quite special. Indeed, we fixed $\theta = 0$ at the top, using the characteristic perturbed conduction equation:

$$(D^2 - a^2)^2 W = -a^2 \theta \mathrm{Ra}$$

$$(3.14)$$

This will lead to the classical equation:

$$D^4 W = 0 \,|\, z = \frac{1}{2}$$

However, for the bottom boundary conditions, we just used an insulated boundary, leading to $\partial_z \theta = 0$. Using 3.14, this easily leads to the following constraints:

$$D^5 W - 2D^3 W a^2 + a^4 DW = 0 \,|\, z = -\frac{1}{2}$$

$$(3.15)$$

Sparrow [4] showed that this typical boundary layer effect has a non-trivial impact on the sets of eigenfunctions we will uncover, and that there is no analytical way of dealing with it simply. This is why, for this kind of non-classical boundary conditions, numerical methods are preferred. However, Sparrow mostly discusses radiative flux at the boundary and does not delve too much into the simple insulated case.

Indeed, just considering the simple fixed temperature case, this will lead to:

$$D^4 W = D^2 W = W = 0 \,|\, z = -\frac{1}{2}, \frac{1}{2}$$

$$(3.16)$$

One can notice that a perfectly natural solution is to consider $W = \cos(\pi z)$. For the insulated boundary, sinusoidal solutions are also possible. Indeed, considering $W = \cos(k_z z)$, (3.15) will lead

Andrea Combette | Louis Poitevin

to the following constraints:

$$-k_z^5 + 2k_z^3 a^2 - a^4 k_z = 0 \,|\, z = -\frac{1}{2}$$

$$(3.17)$$

The only root of this order 5 polynomial is $a = \pm k_z$. Hence, the only sinusoidal solutions that can exist must have the same vertical and horizontal wavelength, which is the case in our simulation (see fig.3.10c).

C. Sinusoidal Solutions

a) Insulating Study

Considering this sinusoidal solution, we can write from (3.12) and considering the complete set of eigenfunctions W_j:

$$W_j = \cos(j\pi z)$$

verifying the boundary conditions (3.13, 3.16). Hence, the only a reachable is $a = \pm j\pi$. The main consequence we may highlight is the quantification of the horizontal mode by the vertical mode (as opposed to the continuous spectrum in the free-free case). One could see that we did not use the characteristic equations to find the fastest growing mode (3.12), because there are only a few sets of allowed modes in our case. However, if we derived the expression of s using the characteristic equation, we obtained for our set of W_j:

$$s = \frac{a^2 \mathrm{Ra}}{(j^2\pi^2 + a^2)^2} - (j^2\pi^2 + a^2)$$

$$(3.18)$$

The fastest growing mode then verifies $\partial_a s = 0$. This a will obviously depend on Ra; however, we can show that for sufficiently high Ra, this dependency can be neglected, and we will have a maximum positive s for a_{max} verifying:

$$a = j\pi$$

Hence, the only modes we can select by imposing insulating boundary conditions and sinusoidal modes are, for sufficiently high Rayleigh, the fastest growing modes in the traditional Rayleigh-Bénard study ($\theta = 0$ at the top and the bottom).
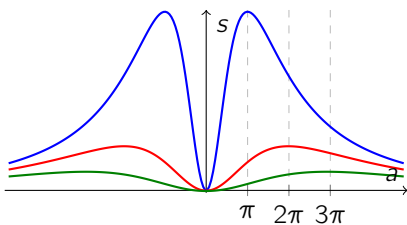

Figure 3.9 – Plot of s for $\mathrm{Ra} = 10^6$, in blue the first $j = 1$ mode, in red the $j = 2$ mode and in red the $j = 3$ mode

b) Free-Free Study

For this traditional case, we may want to seek the maximal condition $\partial_z s = 0$ from (3.18), giving the fastest growing instability mode:

$$X^3 + \mathrm{Ra}X - 2\mathrm{Ra}j^2\pi^2 = 0$$

$$(3.19)$$

With $X = a^2 + j^2\pi^2$, solving this equation is quite heavy analytically using Cardano's formulae and leads to the following enclosed form of the real roots:

$$a = \pm\sqrt{\left[-\pi^2 j^2 \quad + \right.}$$

$$\frac{\left(\sqrt{3}\sqrt{27\pi^4 j^4 R^2 + R^3} + 9\pi^2 j^2 R\right)^{1/3}}{3^{2/3}} -$$

$$\left.\frac{R}{3^{1/3}\left(\sqrt{3}\sqrt{27\pi^4 j^4 R^2 + R^3} + 9\pi^2 j^2 R\right)^{1/3}}\right]$$

We can verify that for $\mathrm{Ra} \gg 1$, we have a maximum growth rate at $a = j\pi$. It is interesting to notice that this does not correspond to the wavelength of the first mode appearing at the onset of the instabilities. Indeed, the approach we made leads to

$$a \overset{\mathrm{Ra}\to\infty}{=} j\pi + O(\frac{1}{\mathrm{Ra}})$$

$$(3.20)$$

It's quite easy to show (taking $\mathrm{Ra}_x = 657.5$) that this mode near the onset of the instability corresponds exactly to the "first" unstable mode verifying

$$a(\mathrm{Ra} = \mathrm{Ra}_c) = \frac{\pi}{\sqrt{2}}$$

$$(3.21)$$

This development for the free-free boundary layer with fixed temperatures showed that the first unstable mode is in fact the fastest one, with, at high Ra, a self-similarity of the solution between our insulated case and the fixed temperature one. The rigid–rigid or mixed case revealed other kinds of anti-symmetric solutions. Hence, we lost our previous explicit solutions and will need numerical calculations [4, 5].

D. Numerical Results

This careful study was mainly motivated by the following results, where we identify, for our Rayleigh number $10^4 \sim 10^6$, a modal excitation that was not in the range of the predicted one at the onset of the instabilities for free-free boundaries (3.21). We did not realize at that time that the thermal boundary conditions were not exactly the same in

our study. The observations were made at different times observing the vorticity

$$\zeta = \nabla \times_z \boldsymbol{u}$$

at a specific height of the fluid for the horizontal dependency, and at a specific horizontal position for the vertical dependency. This was done before the overturn for fig.3.10a, and during the overturn for fig.3.10b.
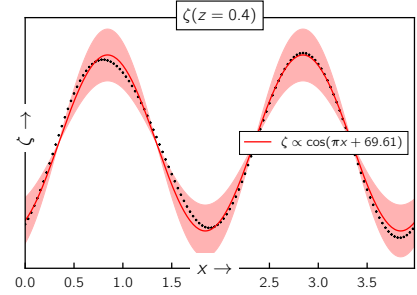
(a) – Scatter plots of the vorticity average over the depth before the overturn and the corresponding fit and error in red
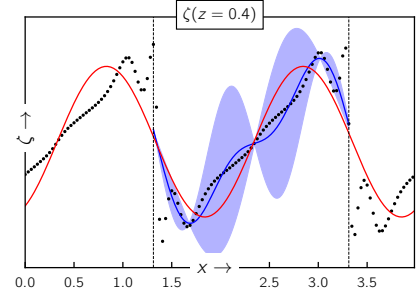
(b) – Scatter plots of the vorticity at $z = 0.4$ during the overturn and the corresponding fit and error in blue, the red fit is for the fast growing mode of wavelength π.
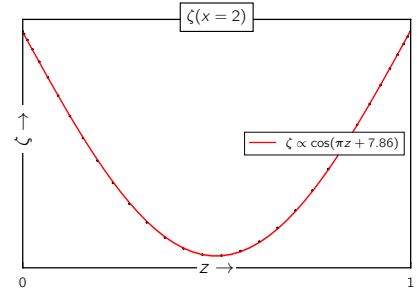
(c) – Scatter plots of the vorticity at $x = 2$ in the same condition as in fig.3.10a. We recover the expected π wavelength

Figure 3.10 – Wavelength of the first and second unstable mode measured in our simulations in the z and x direction

This leads to the expected results with a first growing mode of wavelength π and the second of wavelength 2π. The second fit is not so precise and exhibits large errors due to the growth of other

Andrea Combette | Louis Poitevin

harmonic modes at the same time. We previously said that the wavelength of the instability should be the same in the z direction due to the insulated boundary. This is easily verified in the fig.3.10c.

Now that we verified that the modes unearthed corresponded to the theoretical approach. We can study their growth. To have quick overview of how the growth rate scales with the mode number and the Rayleigh we computed possible modes and their scaling using 3.18. First, one can notice that not all of the wave numbers can be unstable depending on the Rayleigh number. However, one can notice that the number of unstable wavelengths scales rapidly with the increasing Ra, allowing many more unstable wavelengths of decreasing scale (the larger s is, the more a is spread).
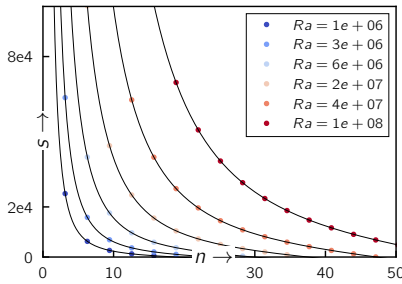
(a) – Growth scale over mode number for different Rayleigh's number.
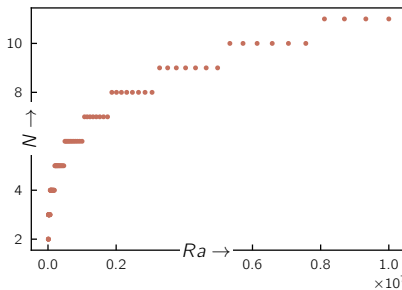
(b) – Number of unstable modes allowed for a given Rayleigh number

Figure 3.11 – Modal analysis of the free-free boundary conditions with one fixed temperature boundary and one insulated boundary

This wide spectrum of unstable modes can be an explanation for the overturn cascade. Indeed, the higher the mode, the slower the growth (see fig.3.11a). Hence, secondary overturns are possible and will maintain a convective behavior much longer than expected, possibly explaining the slow decay scaling in time of $\Phi_{z=0}^{tot}$.

III. Overturn time and scaling

One can be motivated to show that the overturn time corresponds to the first mode's growth rate. Indeed, we expressed previously the growth rate s as a function of the wave number and Ra. We can then compare it to the overturn time. Indeed, we expect to have:

$$\tau_{OV} \approx \frac{1}{s}(n = 1)$$

Since the first mode will be the most unstable. For this, we took the time of the maximum Reynolds number in our simulations and compared it to the characteristic growth time $1/s$. We took the Reynolds number rather than the Nusselt number since the Nusselt number presents a temporal shift, probably due to the diffusion time in the boundary layer. This leads to an almost perfect linear dependency as depicted in fig.3.12. However, a surprising factor of 12.5 is unearthed in the scaling.
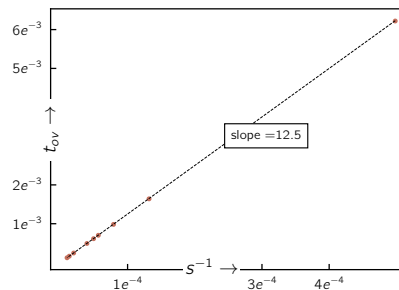

Figure 3.12 – Predicted overturn time in the modal theory and measured time Reynolds number maximum, in our simulations

From this, we can draw some simple conclusions: We found a way to determine theoretically the time of the overturn, and despite this factor that is still unexplained, the overturn time we consider in the moon corresponds to a Rayleigh number of $\sim 10^5, 10^7$, matching quite closely the simulated one (1 order of magnitude below). This overturn time is much longer than expected. Indeed, if we rescale the time, we find:

$$\frac{1}{s} \approx 1 - 10 \text{Myr}$$

The difference between the analytical and simulation results could be found in the noise ratio used in the simulation. In the previous study, the time before the overturn was supposed to be several thousand years, allowing us to neglect the diffusion (2.1). However, this is not the case, and the diffusion should be taken into account in the model established in the previous studies.

In the first part of this study, we explored the effects of two control parameters of the overturn that occurred in the cumulates of the Moon at the beginning of the second cooling phase: the shape of the profile through a piecewise linear function mimicking the $1/r^3$ profile, and two different values of the Rayleigh number, one allowing us to better understand the dynamics of the overturn and the other providing actual results on the events that occurred on the Moon.

We found that, though the shape varies up to the linear approximation, the energy dissipated in the LMO remains constant, only affected by the Ra, which reduces it as it increases. However, we found that the kinematics of the overturn were strongly affected by the choice of e, as an entire order of magnitude separates the overturn times between the shallow simulations and the deep ones. The internal dynamics are also strongly affected as the local internal flux varies by several orders of magnitude between the shallow and the deep simulations.

In the end, we found that the overturn occurred somewhere between 23 Myr and 115 Myr after the end of the first cooling stage, and it spans between 4.5 Myr and 35 Myr, transferring an energy of the order of 6 Exa-Joules to the LMO.

In the second part of our study, we highlighted the impact of the Rayleigh number on the dynamics, with a first convective behavior, unearthing boundary layer structures leading to a specific scaling of the external flux over the Rayleigh number. We proposed a model linking the overturn time to the growth rate of the fastest growing mode, which matches the observed overturn time, albeit with a surprising factor.

Finally, we discussed the implications of our findings for future models, including the need to account for diffusion effects in future simulations, which could explain the discrepancy between analytical and simulated overturn times.

Bibliography

1. Colin, L., Michaut, C., Labrosse, S. & Bourdon, B. Thermal evolution of the lunar magma ocean. *Earth and Planetary Science Letters* **648,** 119109. ISSN: 0012-821X. https : / / www . sciencedirect . com / science / article / pii / S0012821X24005417 (2024).

Andrea Combette | Louis Poitevin

2. Burns, K. J., Vasil, G. M., Oishi, J. S., Lecoanet, D. & Brown, B. P. Dedalus: A flexible framework for numerical simulations with spectral methods. *Physical Review Research* **2,** 023068. arXiv: 1905 . 10388 [astro-ph.IM] (Apr. 2020).

3. Drazin, P. G. & Reid, W. H. *Hydrodynamic Stability* 2nd ed. (Cambridge University Press, 2004).

4. Sparrow, E. M., Goldstein, R. J. & Jonsson, V. K. Thermal instability in a horizontal fluid layer: effect of boundary conditions and non-linear temperature profile. *Journal of Fluid Mechanics* **18,** 513–528 (1964).

5. Chandrasekhar, S. *Hydrodynamic and hydromagnetic stability* Dover ed. (New York (N.Y.) : Dover publications, 1981, c1961., Dover ed.1981).

6. Stéphane Labrosse Chloé Michaut, T. A. *Elements of geodynamics* 2024.

Andrea Combette | Louis Poitevin